Assessment of Rotor Hover Performance Using a Node-based Flow Solver

Mun Seung Jung* and Oh Joon Kwon**
Korea Advanced Institute of Science and Technology
335 Gwahangno, Yuseong-gu, Daejeon 305-701, Korea

Hee Jung Kang***
Korea Aerospace Research Institute
115 Gwahangno, Yuseong-gu, Daejeon 305-333, Korea

Abstract

A three-dimensional viscous flow solver has been developed for the prediction of the aerodynamic performance of hovering helicopter rotor blades using unstructured hybrid meshes. The flow solver utilized a vertex-centered finite-volume scheme that is based on the Roe's flux-difference splitting with an implicit Jacobi/Gauss-Seidel time integration. The eddy viscosity are estimated by the Spalart-Allmaras one-equation turbulence model. Calculations were performed at three operating conditions with varying tip Mach number and collective pitch setting for the Caradonna-Tung rotor in hover. Additional computations are made for the UH-60A rotor in hover. Reasonable agreements were obtained between the present results and the experiment in both blade loading and overall rotor performance. It was demonstrated that the present vertex-centered flow solver is an efficient and accurate tool for the assessment of rotor performance in hover.

Key Word : Unstructured hybrid meshes, Vertex-centered finite-volume scheme, Rotor performance, Viscous flows

Introduction

In recent years, unstructured mesh techniques have become increasingly more popular, because of its advantages, such as the flexibility in handling complex configurations and the ability of adopting a solution-adaptive mesh refinement. However, application of unstructured mesh techniques has been mostly limited to inviscid flows and low-Reynolds number viscous flow problems. One of the reasons is that high-Reynolds number flows require excessively large number of cells when isotropic cell elements are used to resolve the thin boundary layer near the wall surface. The use of highly stretched tetrahedral cells, instead of isotropic tetrahedral elements, sometimes degrades the robustness of the flow solver and ends up in an inaccurate solution, because the computational cells do not align properly with the flow direction.

An alternative approach for the unstructured mesh topology is to use hybrid meshes, which are composed of semi-structured prismatic cells inside the boundary layer and isotropic tetrahedral cells for the rest of the computational domain[1,2]. When the aspect ratio of the prismatic elements becomes very large in the order of $10^4 \sim 10^6$, the numerical behavior of the flow solver becomes very poor. Therefore it is important to adopt a numerical scheme that is stable and robust not only on isotropic cells but also on highly-stretched high-aspect ratio cells.

* Graduate Research Assistant, Aerospace Engineering
** Professor, Aerospace Engineering
E-mail : ojkwon@kaist.ac.kr Tel : 042-869-3720 Fax : 042-869-3710
*** Senior Research Engineer, Rotor Department, Aeronautics Program Office

Even though several researches have been successfully performed for hovering rotor using inviscid methods, the capability of handling viscosity is still a very desirable feature for the simulation of realistic flows. It is particularly true for the accurate simulation of viscous-inviscid interaction involving shock-induced separation at transonic tip Mach number with relatively high collective pitch setting. Several viscous flow simulations have been performed to predict the rotor performance on structured and unstructured grids. Srinivasan et al.[3] described one of the earliest viscous flow simulations using a single-block. The results showed good agreement with the experimental pressure distribution and the tip vortex trajectory. Wake and Beader[4] presented comparisons of the viscous flow predictions to the UH-60A rotor performance data. The results included spanwise loading distribution, overall thrust, torque, and Figure of Merit over a range of collective pitch angles. Ahmad and Strawn[5] used a structured overset grid viscous flow method to investigate the dependency of three different wake grid resolutions. Kang and Kwon[6] used the multi-level mesh adaption technique on cell-centered unstructured tetrahedral grid and showed that the tip vortex trajectory and its strength can be accurately captured.

Usually, it is known that vertex-centered schemes are more robust and less affected by the grid quality than cell-centered schemes, because more stencils are involved in resolving the convective and diffusive fluxes. Also, vertex-centered schemes work well on hybrid meshes, because they are based on an edge-data structure and thus are irrelevant to cell types.

Even though successful simulation of viscous flow fields has been made for fixed wing aircrafts on unstructured hybrid meshes, rare applications were made to the rotary wings.

In the present study, a vertex-centered unstructured hybrid mesh solver has been developed for the simulation of hovering rotor in viscous flow fields. The governing Reynolds-averaged Navier-Stokes equations were discretized using a finite- volume method in conjunction with Roe's flux-difference splitting. An implicit Jacobi/Gauss-Seidel method was used for time integration. The Spalart-Allmaras one-equation turbulence model was used to estimate eddy viscosity. The flow solver was parallelized by adopting a domain decomposition strategy to reduce the computation time. For the validation of the flow solver, calculations were made for the experimental hovering rotor by Caradonna-Tung[7]. Additional computations were made for the hovering UH-60A rotor[8].

Numerical Method

2.1 Discretization of governing equations

The equations governing three-dimensional, viscous, unsteady, compressible flows are the Reynolds-averaged Navier-Stokes equations, which can be recast by using absolute flow variables on a rotational frame of reference in an integral form for a bounded domain V with a boundary ∂V ;

$$\frac{\partial}{\partial t}\iiint_V Q\,dV+\iint_{\partial V} F(Q)\cdot\vec{n}\,dS=\iint_{\partial V} G(Q)\cdot\vec{n}\,dS+\iiint_V S(Q)\,dV \tag{1}$$

where $Q=[\rho,\ \rho u,\ \rho v,\ \rho w,\ e_0]$ is the solution vector of conservative variables for the mass, momentum and energy equations. The governing equations were discretized using a vertex-centered finite-volume method. The flow domain was divided into a finite number of control volumes surrounding each vertex made of a non-overlapping median-dual cell whose boundary surfaces were defined by the cell centroid, face centroid, and mid-point of the edge as shown in Fig.1(a). In order to reduce the computational overhead involved with the flux evaluation, an equivalent flat surface, given by the sum of the vectors representing all triangles assigned to each edge, was taken, instead of calculating fluxes through individual triangles assigned to the edge, as shown in Fig.1(b). The volume was calculated using the divergence theorem[9], which allows to treat different types of cell elements in a simple and accurate manner.

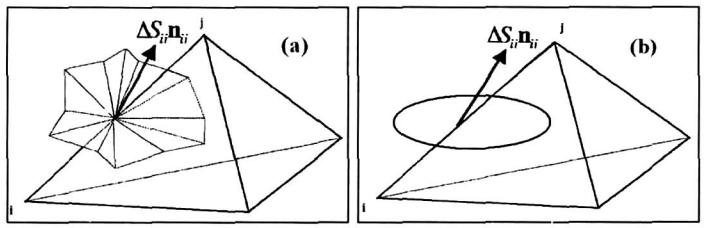

Fig. 1. Median-dual control volume

The inviscid flux term, $F(Q)$, was computed using Roe's flux-difference splitting scheme. The flow variables at each dual face were computed by using a linear reconstruction approach for second-order spatial accuracy. In this approach, the face value of the primitive variables was calculated from surrounding vertices using the averaged solution gradient of each control volume obtained from a least-square procedure[10]. Venkatakrishnan's limiter[11] was adopted to reduce the numerical oscillation in transonic flow. The second-order derivatives of the viscous terms are evaluated by the Green-Gauss theorem, and the viscous flux term, $G(Q)$, was computed by adopting a modified central differencing[12] to prevent the odd-even decoupling problem. The source term, $S(Q)=[0,\ \Omega\rho v,\ -\Omega\rho u,\ 0,\ 0]$, was to account for the centrifugal acceleration of the rotating blade about the axis of rotation. An implicit time integration algorithm based on a linearized second-order Euler backward difference was used to advance the solution in time. The linear system of equations was solved at each time step using a point Gauss-Seidel method.

The Spalart-Allmaras one-equation turbulence model[13] was used to estimate the eddy viscosity. In the present implementation, the turbulent model equation was solved separately from the mean flow equations. The source and convection terms were implemented as suggested by the model developer, and the diffusion terms were discretized and integrated in time in a same manner to the mean flow equations.

The conservation property of flow is required to prevent unphysical mass, momentum or energy generation in the numerical solution. For the preservation of uniform freestream, the following equation relationship can be induced from equation (1);

$$\frac{\partial V}{\partial t}=\sum_{f}\overrightarrow{V_g}\cdot\vec{n}\,dS \tag{2}$$

which is referred as the Geometric Conservation Law[14]. This represents that temporal volume variation should be balanced with the surface integral of the grid velocity V_g, Because there is no control volume variation in the present study, the grid velocity has to be conserved by itself. In order to guarantee the GCL, the grid velocity was computed at each triangle center and was transformed to the flat surface in a similar manner to the computation of an equivalent flat surface. The present implementation provided the same grid velocity to the method based on volume sweep by each face[15], but at a much reduced computational cost.

2.2 Boundary condition

To predict viscous boundary layer flow accurately and to eliminate the numerical error, the no-slip and the isothermal boundary conditions were imposed at the solid wall as suggested by Anderson and Bouhaus[16].

At the far-field boundary, the flux was computed using flow quantities from the adjacent vertices and the freestream value determined as suggested by Srinivasan *et al*[3]. In this method, 1-D momentum theory was used to approximate the inflow/outflow boundary conditions by introducing a 3-D point sink concept.

Due to the periodic nature of the flow for hovering rotors, calculations were performed for single blade of the rotor and the periodic boundary condition was applied between the blades. The grid periodicity was enforced in the grid generation process, and the vertices adjacent to this boundary were treated as interior vertices by adding artificial vertex stencils.

At the far-field boundary, the value of working variable, $\tilde{\nu}$, for the Spalart-Allmaras turbulence equation was extrapolated from the interior for outflow and was specified to be the freestream value for inflow. The intensity of freestream turbulence was taken to be 10% of the laminar viscosity.

The initial condition may be set equal to the freestream state everywhere.

2.3 Parallel implementation

To reduce the large computational time and the excessive memory requirement, a parallel algorithm based on a domain decomposition strategy was adopted. The global computational domain filled with mixed elements, such as prism, pyramid and tetrahedron, was converted into a nodal graph according to an edge-data structure. Next, the nodal-graph was partitioned by using the MeTiS library[17]. The Message Passing Interface was used to exchange the updated flow variables across the edges that straddle two adjacent mesh partitions. For the vertices that were accessed by the edges in the adjacent subdomain, ghost vertices were allocated in each subdomain. So that fluxes and flux jacobians were evaluated along the edges and were summed up to the vertices with transferred flow variables at the ghost vertices without additional communication. Then, the flow values at the vertices were exchanged for the Gauss-Seidel iteration. The newly updated flow variables were finally transferred to the ghost vertices in the adjacent subdomain.

All calculations were performed on PC-based Linux clusters.

Results and Discussion

3.1 Caradonna-Tung rotor in hover

The first validation of the present method was made to the experimental hovering rotor of Caradonna-Tung[7]. The experimental model had a two-bladed, untwisted, rigid rotor. The blades were made of an NACA0012 airfoil section with a rectangular planform of an aspect ratio of six. Three hovering flight conditions were chosen from the experimental data for the calculations: 1) tip Mach number $M_{Tip}= 0.439$, collective pitch angle $\theta_c=8^o$, and the Reynolds number based on the blade tip speed and the chord length, $Re=1.92\times10^6$ 2) $M_{Tip}=0.877$, $\theta_c=8^o$, and $Re=3.93\times10^6$ 3) $M_{Tip}=0.794$, $\theta_c=12^o$, and $Re=3.55\times10^6$.

Unstructured hybrid meshes used for the present calculations were generated by using a commercial software Centaur[18]. The far-field boundary was located at five radii upstream and downstream of the rotor and also five radii away from the axis of rotation in the radial direction. The computational domain and the surface triangulations at the computational boundaries are shown in Fig. 2. The grid periodicity can be confirmed at the periodic boundaries between blades in this figure.

The blade surface triangulation and the subdomain boundaries for parallel computing are shown in Fig. 3(a) for the $M_{Tip}= 0.439$ case. A typical sectional view of the prismatic element inside the boundary layer and the tetrahedral elements for the rest of the computational domain at r/R = 0.5 are presented in Fig. 3(b). For the investigation of the viscous effect, inviscid calculations were also conducted. In order to eliminate the dependency on the mesh resolution, the same surface mesh was adopted for both inviscid and viscous flow simulations.

The information about the computational meshes for the three calculation cases is summarized in Table 1. The normal distance of the first vertex away from the blade surface was determined as a function of Reynolds number and tip Mach number for each case. Thin prismatic layers were stacked from the blade surface by marching inside the flow domain. Thirty prisms were generated inside the boundary layer and the height of each prism layer was increased by a ratio of 1.20 for all cases.

Table 1. Characteristics and parameters of the computational mesh for three cases

	$M_{Tip}=0.439,\ \theta_c=8^o,$ $Re=1.92\times10^6$	$M_{Tip}=0.877,\ \theta_c=8^o,$ $Re=3.93\times10^6$	$M_{Tip}=0.794,\ \theta_c=12^o,$ $Re=3.55\times10^6$
Vertices	859,275	1,111,544	1,406,726
Prisms	1,144,540	1,686,450	2,428,500
Tetra.	1,076,075	1,458,764	1,007,281
y_1	1.8×10^{-5}	1.2×10^{-5}	1.5×10^{-5}
y^+	1.02	0.98	1.17

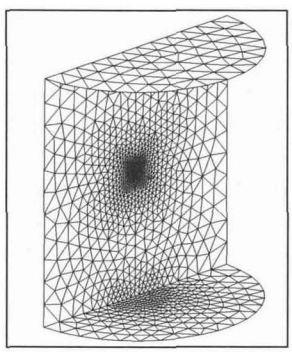

Fig. 2. Surface triangulation at the computational boundaries

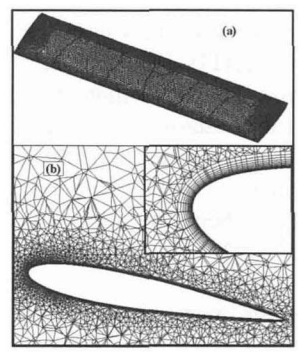

Fig. 3. Blade surface triangulation with parallel domain partitioning (a)and sectional view of the computational mesh at 50% span(b).

The predicted surface pressure distributions are compared with the experimental data[7] in Fig. 4. The results are in good agreement with the experiment at all radial stations of the blade. For the subsonic tip Mach number of 0.439, both viscous and inviscid simulations showed almost identical results. At the transonic tip Mach number of 0.877, the location and the strength of the shock wave were captured better by the present viscous simulation due to consideration of the shock-boundary layer interaction, which reduced the shock strength and pushed its position toward the leading-edge of the blade. It is also shown that the results of the viscous calculation are in significantly better agreement with the experimental data than those of the inviscid calculation for high pitch setting of the $M_{Tip}=0.794,\ \theta_c=12^o$ case except at the tip region. This discrepancy of the viscous simulation at the tip region may be due to the strong shock-boundary layer interaction and the locally separated region.

Figure 5 shows the sectional thrust distribution along the blade span. Comparison of the present results with the experiment[7] and the inviscid calculation is presented. The spanwise thrust distributions compared reasonably well with the experimental data up to r/R = 0.85. However, the numerical simulations near the tip blade were predicted lower than the experiment. The viscous simulation predicted slightly less blade loading than the inviscid calculation at the outboard of the blade due to the viscous loss mechanism.

Table 2. Comparison of total thrust coefficient

	$M_{Tip}=0.439$	$M_{Tip}=0.877$	$M_{Tip}=0.794$
Experiment	0.00459	0.00473	0.00792
Viscous	0.00473	0.00478	0.00814
Inviscid	0.00498	0.00510	0.00874

The total thrust coefficients of all simulation cases are compared in Table. 2. The estimated thrust coefficients from the viscous simulation show reasonable agreement with the experiment and are slightly lower than inviscid simulations, which is consistent with the results observed in the Fig. 5.

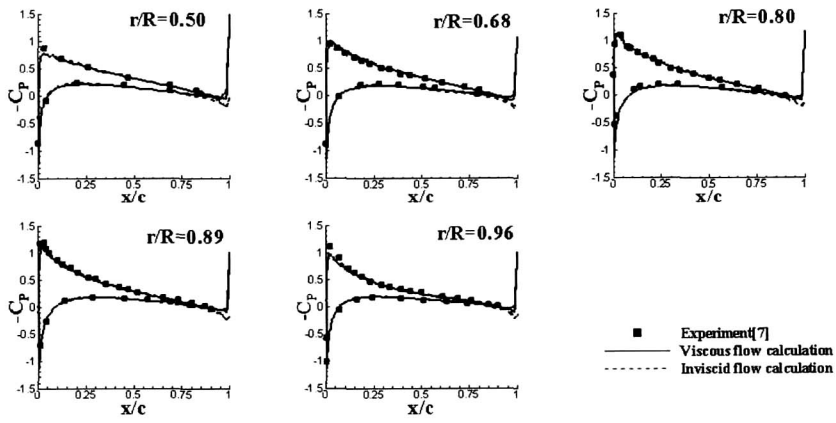

(a) $M_{Tip}=0.439,\ \theta_c=8^o,\ Re=1.92\times10^6$

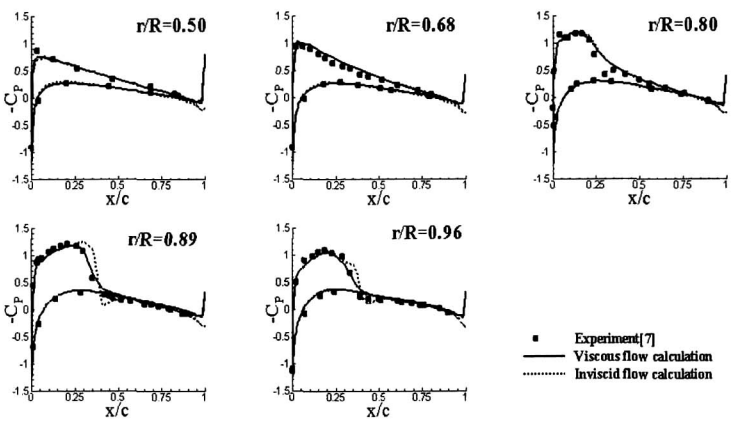

(b) $M_{Tip}=0.877,\ \theta_c=8^o,\ Re=3.93\times10^6$

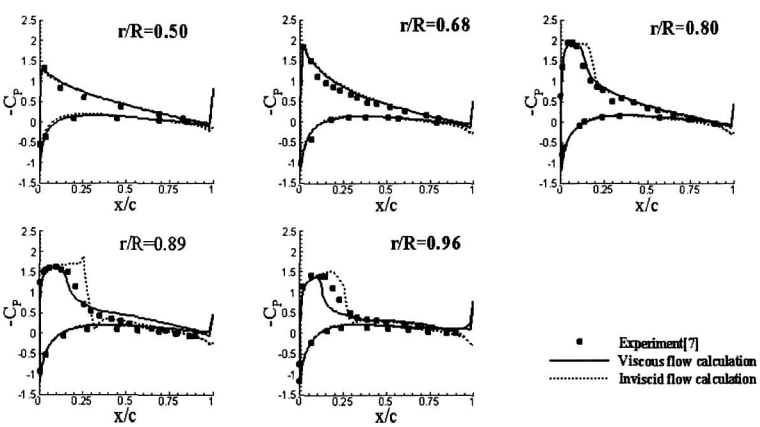

(c) $M_{Tip}=0.794,\ \theta_c=12^o,\ Re=3.55\times10^6$

Fig. 4. Comparison of chordwise surface pressure distributions at three flight conditions

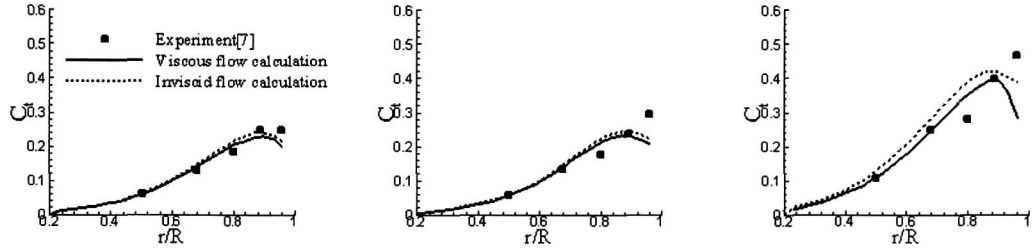

Fig. 5. Spanwise sectional thrust loading distributions

3.2 UH-60A rotor in hover

The second application of the present method was made to a hovering UH-60A main rotor[8]. The experimental model had a four-bladed, twisted, flexible rotor. The blades were made of two airfoil sections, the 9.5% thick SC-1095 and the SC-1094 R8. The blade had a 20 degree rearward sweep that begins at r/R=0.93 without taper. The blade had a non-linear twist at the tip and the maximum twist angle was -13.3^{o}. The UH-60A rotor blade had an aspect ratio of 15.51 and a geometric solidity of 0.0826[19]. Among the various measurement cases reported in the experiment, the calculations were made at a blade tip Mach number of 0.65 and the Reynolds number of 2.95×10^{6} with several collective pitch angles of 4.25^{o}, 7.3^{o}, 10.47^{o} and 11.81^{o}.

The computational domain and the surface triangulation at the computational boundaries are shown in Fig. 6. The far-field boundary is located at five radii upstream, downstream and radial direction. The computational domain was consisted of 1,725,618 vertices, 2,803,140 prisms and 1,755,768 tetrahedra. The initial thickness of the prism layer was 1.2×10^{-5} of the blade root chord length, which was approximately equivalent to $y^{+}\approx1$ for all cases. Thirty prismatic layers were stacked from the blade surface with an 1.25 increment ratio of the layer height.

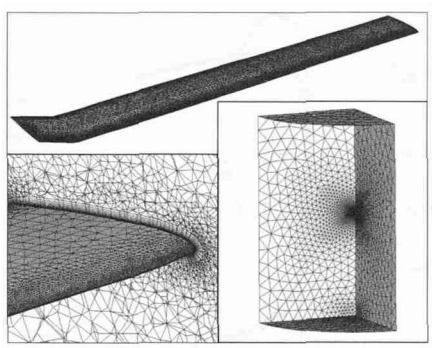

Fig. 6. Surface triangulation at the computational boundaries and sectional view at r/R=0.93

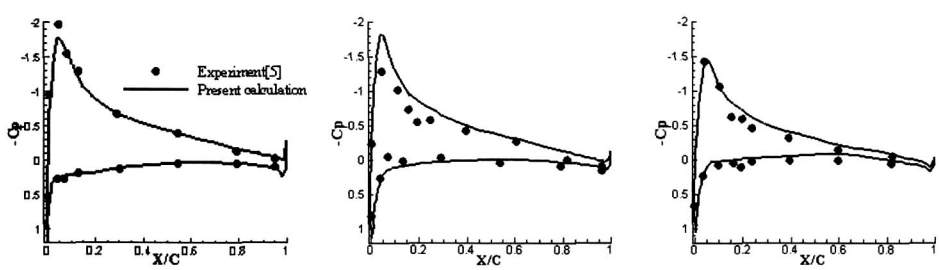

Fig. 7. Comparison of surface pressure distributions on the blade of UH-60A at $\theta_c=10.47^{o}$

In Fig. 7, the surface pressure distributions on the rotor blade are presented at $\theta_c = 10.47^o$ pitch angle. Even though the blade elastic twist effect was not considered, reasonable comparison was obtained between the present calculation and the experiment for all selected locations. In Fig. 8, the sectional thrust loading from the present calculation was compared with the measured experimental data. Good agreement was obtained at the inboard section of the blade. However, over-predicted results was obtained at the region outside r/R=0.7. This is due to low estimated downwash velocity, which may be related with inaccurate strength and location of passing vortex.

The predicted thrust coefficient, C_T/σ, versus collective pitch angle, θ_c, is presented in Fig. 9. It shows that the predicted thrust is consistently higher than the experimental data, which is due to the over-estimation of the thrust near the tip regions, as shown in Fig. 8. The predicted torque coefficient, C_Q/σ, versus C_T/σ is presented in Fig. 10. A similar trend is also shown between the experimental and the computational results. For the collective pitch angle of 4.25^o, the computed torque coefficient showed a lower value than that of the experiment at given thrust. The Figure of Merit (FM) comparison is presented in Fig. 11. Because of the under-predicted torque coefficient, the Figure of Merit was about 0.07 point over-estimated for the collective pitch angle of 4.25^o. At other collective pitch settings, the predicted results are in fair agreement with the experiment with less than 0.03 point difference.

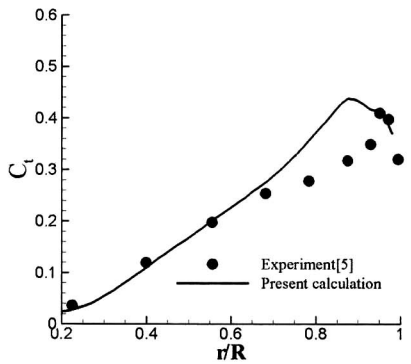

Fig. 8. Sectional thrust loading distribution along the spanwise direction of UH-60A rotor at $\theta_c = 10.47^o$

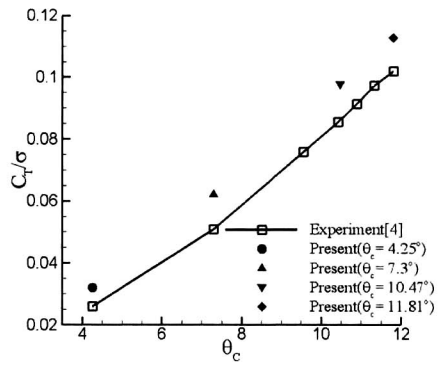

Fig. 9. Comparison of collective pitch, θ_c, versus thrust coefficient, C_T/σ, for the UH-60A rotor

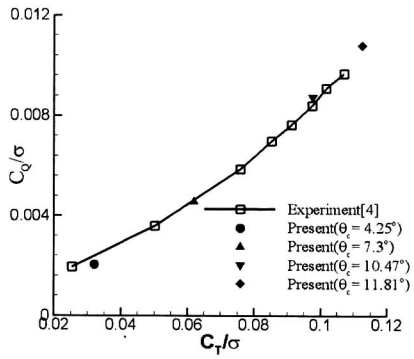

Fig. 10. Comparison of thrust predictions, C_T/σ, versus torque coefficient, C_Q/σ, for the UH-60A rotor

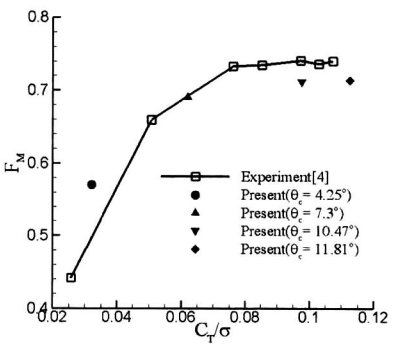

Fig. 11. Comparison of thrust predictions, C_T/σ, versus Figure of Merit for the UH-60A rotor

Conclusions

A three-dimensional vertex-centered viscous flow solver based on an unstructured hybrid mesh methodology has been developed for the prediction of the aerodynamic performance of hovering rotor blades. For validation, the present method was applied to two rotor configurations; the Caradonna-Tung and UH-60A rotor. For the Caradonna-Tung rotor, calculations were performed at three different operating conditions with different tip Mach number, collective pitch setting and Reynolds number. Comparisons of the inviscid and viscous results indicated that inclusion of viscosity significantly affects the surface pressures and the blade airloads for transonic tip Mach number cases. For the UH-60A rotor, calculations showed reasonable comparisons of the surface pressure distribution with the experiment. The predicted rotor performance also showed comparable results. It was demonstrated that the present method is efficient and reliable for the simulation of viscous flows around hovering helicopter rotors.

Acknowledgement

This study has been supported by the KARI under KHP Dual-Use Component Development Program funded by the MOCIE.

References

1. Kallinderis, Y., 1996, "A 3-D Finite-Volume Method for the Navier-Stokes Equations with Adaptive Hybrid Grids", *Applied Numerical Mathematics*, Vol. 20, No. 4, pp. 389-406.

2. Mavriplis, D. J. and Venkatakrishnan, V., 1995, "A Unified Multigrid Navier-Stokes Equations on Mixed Element Meshes", *ICASE Report No. 95-5.*

3. Srinivasan, G. R., Beader, J. D., Obayashi, S. and McCroskey, W. J., 1992, "Flow Field of a Lifting Rotor in Hover : A Navier-Stokes Simulation", *AIAA Journal*, Vol. 30, No. 10, pp. 2371-2378.

4. Wake, B. E. and Beader, J. D., 1996, "Evaluation of a Navier-Stokes Analysis Method for Hover Performance Prediction", *Journal of the American Helicopter Society*, Vol. 41, No. 1, pp. 7-17.

5. Ahmad, J. U. and Strawn, R. C., May 1999, "Hovering Rotor and Wake Calculations with an Overset-Grid Navier-Stokes Solver", *American Helicopter Society 55th Annual Forum*, Montreal, Canada.

6. Kang, H. J. and Kwon, O. J., 2002, "Unstructured Mesh Navier-Stokes Calculations of the Flow Field of a Helicopter Rotor Hover", *Journal of the American Helicopter Society*, Vol. 47, No. 2, pp.90-99.

7. Caradonna, F. X. and Tung, C., 1981, "Experimental and Analytical Studies of a Model Helicopter Rotor in Hover", *NASA TM 81232.*

8. Shinoda, P. M, Yeo, H. and Norman, T. R., June 2002, "Rotor Performance of a UH-60 Rotor System in the NASA Ames 80- by 120-Foot Wind Tunnel", *American Helicopter Society 58th Annual Forum*, Montreal, Canada.

9. Bruner, C. W. S, 1995, "Geometric Properties of Arbitrary Polyhedra in Terms of Face Geometry", *AIAA Journal*, Vol. 33, No. 7, p.1350.

10. Haselbacher, A. and Blazek, J., 2000, "Accurate and Efficient Discretization of Navier-Stokes Equations on Mixed Grids", *AIAA Journal*, Vol. 38, No. 11, pp. 2094-2102.

11. Venkatakrishnan, V., 1995, "Convergence to Steady State Solutions of Euler Equations on Unstructured Grid with Limiters," *Journal of Computational Physics*, Vol. 118, No. 1, pp, 120-130.

12. Mathur, S. R. and Murthy, J. Y., 1997, "A Pressure-Based Method for Unstructured Meshes", *Numerical Heat Transfer*, Part B, Vol. 31, No. 2, pp. 195-215.

13. Spalart, P. R. and Allmaras, S. R., 1992, "A One-Equation Turbulent Model for Aerodynamic Flows", *AIAA paper* 92-0439.

14. Thomas, P. D. and Lombard, C. K., 1979, "Geometric Conservation Law and It's application to Flow Computations on Moving Grid", *AIAA Journal*, Vol. 17, No. 10, pp.1030-1037.

15. Nkonga, B. and Guillard, H., 1994, "Godunov Type Method on Non-Structured Meshes for Three-Dimensional Moving Boundary Problems", *Computer Methods in Applied Mechanics and Engineering*, Vol. 113, No. 1, pp. 183-204.

16. Anderson, W. K. and Bonhaus, D, L., 1994, "An Implicit Upwind Algorithm for Computing Turbulent Flows on Unstructured Grids," *Computers & Fluids*, Vol. 23, No. 1, pp. 1-21.

17. Karypis, G. and Kumar, V., 1998, "Multilevel k-way Partitioning Scheme for IrregularGraphs", *Journal of Parallel and Distributed Computing*, Vol. 48, No. 1, pp. 96-129.

18. www.centaursoft.com

19. Bousman, W. G., 2003, "Aerodynamic Characteristics of SC1095 and SC1094 R8 Airfoils", *NASA/TP-2003 -212265.*